Vimentin coordinates fibroblast proliferation and keratinocyte differentiation in wound healing via TGF-β–Slug signaling

Fang Cheng[a,b], Yue Shen[c,d,e], Ponnuswamy Mohanasundaram[a,b], Michelle Lindström[a], Johanna Ivaska[b,f], Tor Ny[c], and John E. Eriksson[a,b,1]

[a]Cell Biology, Biosciences, Faculty of Science and Engineering, Åbo Akademi University, FI-20520, Turku, Finland; [b]Turku Centre for Biotechnology, University of Turku and Åbo Akademi University, FI-20521, Turku, Finland; [c]Department of Medical Biochemistry and Biophysics, Umeå University, SE-90187 Umeå, Sweden; [d]Centre for Heart Lung Innovation, St. Paul's Hospital, Vancouver, BC, Canada V6Z 1Y6; [e]Department of Pathology and Laboratory Medicine, University of British Columbia, Vancouver, BC, Canada V6Z 1Y6; and [f]Department of Biochemistry and Food Chemistry, University of Turku, FI-20520, Turku, Finland

Edited by Pierre A. Coulombe, The Johns Hopkins University, Baltimore, MD, and accepted by Editorial Board Member Edward D. Korn June 8, 2016 (received for review December 23, 2015)

Vimentin has been shown to be involved in wound healing, but its functional contribution to this process is poorly understood. Here we describe a previously unrecognized function of vimentin in coordinating fibroblast proliferation and keratinocyte differentiation during wound healing. Loss of vimentin led to a severe deficiency in fibroblast growth, which in turn inhibited the activation of two major initiators of epithelial–mesenchymal transition (EMT), TGF-β1 signaling and the Zinc finger transcriptional repressor protein Slug, in vimentin-deficient ($VIM^{-/-}$) wounds. Correspondingly, $VIM^{-/-}$ wounds exhibited loss of EMT-like keratinocyte activation, limited keratinization, and slow reepithelialization. Furthermore, the fibroblast deficiency abolished collagen accumulation in the $VIM^{-/-}$ wounds. Vimentin reconstitution in $VIM^{-/-}$ fibroblasts restored both their proliferation and TGF-β1 production. Similarly, restoring paracrine TGF-β–Slug–EMT signaling reactivated the transdifferentiation of keratinocytes, reviving their migratory properties, a critical feature for efficient healing. Our results demonstrate that vimentin orchestrates the healing by controlling fibroblast proliferation, TGF-β1–Slug signaling, collagen accumulation, and EMT processing, all of which in turn govern the required keratinocyte activation.

vimentin intermediate filaments | wound healing | epithelial–mesenchymal transition | fibroblast proliferation | keratinocyte migration

Successful cutaneous wound repair requires a series of tightly coordinated and overlapping steps including inflammation, new tissue formation, and remodeling (1, 2). Upon injury, keratinocytes at the wound edges form epithelial tongues that move and interact with the dermal cells and collagen-rich extracellular matrix (ECM) to reestablish coverage of the wound bed via a complex process termed "reepithelialization" (2, 3). In addition, dermal fibroblasts activated by growth factors migrate into the site of injury, where they proliferate and lay down the ECM that facilitates cell migration and tissue reconstruction (2, 3).

To migrate over the wound site, keratinocytes must disengage desmosome/hemidesmosome junctions and reorganize their cytoskeleton to enable the required promigratory program (4). As reepithelialization continues, keratinocytes gradually stop migration, revert to their normal phenotype, and use hemidesmosomes to attach firmly to the reestablished basement membrane and to the underlying dermis through collagen fibrils (1, 2, 5). Some of these dramatic phenotypic changes reflect the transformation of the epithelial cells to a mesenchymal state, a critical differentiation program called "epithelial–mesenchymal transition" (EMT). During EMT, epithelial cells lose their intercellular junctions and acquire mesenchymal phenotypes as manifested, for example, by increased motility and increased production of ECM. EMT is a process that is crucial for cells requiring a shift from an epithelial state toward a more dynamic state. In addition to wound healing, EMT is involved in embryonic development, fibrosis, and tumor progression (6, 7).

The intermediate filament protein vimentin participates in numerous cellular processes, with functions in cell adhesion, migration and invasion, signaling, differentiation, cytoskeletal rearrangements, and regulation of cell morphology and plasticity (8–11). Recent data from our consortium have shown that vimentin is required to support ERK-mediated Slug phosphorylation and activation in a cancer-related model (12). With this model, we could show that vimentin–ERK–Slug interaction amplifies EMT onset via a positive-feedback loop between vimentin and the transcription factor Slug, which has an established role in skin development and the EMT-like processes of wound healing (13–15).

In relation to tissue repair, vimentin has been found in mesenchymal repair cells to regulate the collective movement of the lens epithelium in response to an injury (16). In relation to vimentin's role in maintaining lens homeostasis and integrity, vimentin mutations have also been linked with cataract formation (17, 18). Furthermore, we have demonstrated previously that vimentin is required in inflammatory cell migration; vimentin-deficient lymphocytes have a reduced transmigration capability in vivo because of the down-regulation of the adhesion molecule ICAM-1 and integrins on the cell surface (19). Although the original report on vimentin-knockout ($VIM^{-/-}$) mice reported no defects in tissue repair (20), later studies revealed defective fibroblast migration and hampered contractile capacity of fibroblasts during wound healing in $VIM^{-/-}$ embryonic

Significance

The central concept in this study is that a major cytoskeletal component, vimentin, acts as a signal integrator during wound healing, operating in both signal-triggering and signal-receiving cells. This is a previously unreported concept for intermediate filaments, with an evolving paradigm according to which intermediate filaments emerge as integrators of regeneration with specific functions in the particular tissues for which individual intermediate filaments are characteristic. Our study reveals the underlying molecular and cellular control functions of vimentin in vimentin-dependent epithelial–mesenchymal transition, regeneration, and healing.

Author contributions: F.C., J.I., and J.E.E. designed research; F.C., Y.S., P.M., and M.L. performed research; J.I. and T.N. contributed new reagents/analytic tools; F.C., Y.S., P.M., and M.L. analyzed data; and F.C. and J.E.E. wrote the paper.

The authors declare no conflict of interest.

This article is a PNAS Direct Submission. P.A.C. is a guest editor invited by the Editorial Board.

Freely available online through the PNAS open access option.

[1]To whom correspondence should be addressed. Email: john.eriksson@abo.fi.

This article contains supporting information online at www.pnas.org/lookup/suppl/doi:10.1073/pnas.1519197113/-/DCSupplemental.

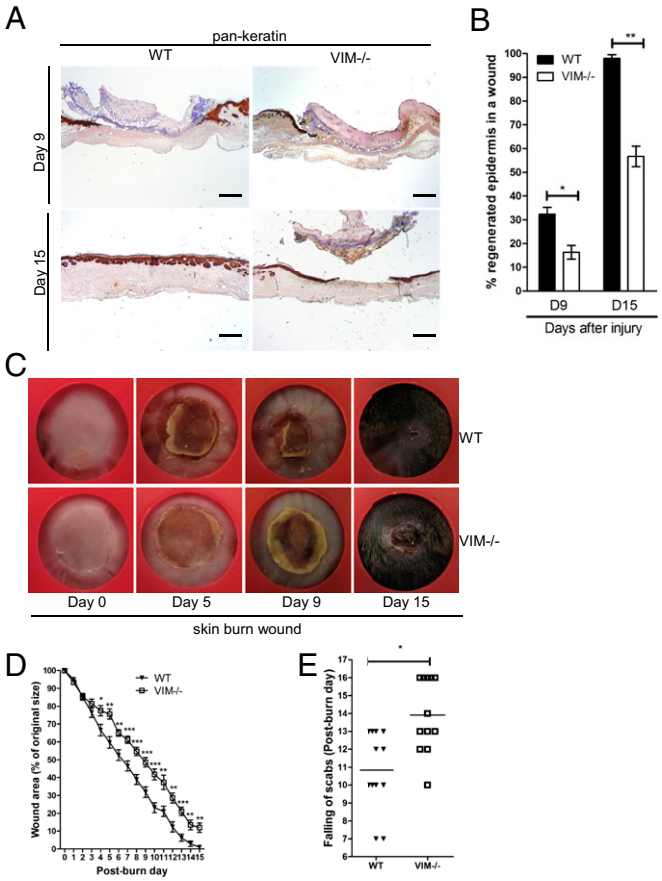

Fig. 1. VIM$^{-/-}$ mice display wound-healing defect in a burn wound model. (*A*) Representative pictures showing immunohistochemical labeling of pan-keratin in WT and VIM$^{-/-}$ wounds on days 9 (D9) and 15 (D15) postinjury. (Scale bar, 100 μm.) (*B*) Quantification of the percentage of wound reepithelialization at different time points after wounding in VIM$^{-/-}$ and WT wounds. Data are shown as means ± SEM; $n = 6$. (*C*) Representative wound pictures from VIM$^{-/-}$ and WT mice during the 15-d wound-healing period. (*D*) Quantification of the remaining wound area at different time points after wounding in WT and VIM$^{-/-}$ groups. Data are shown as means ± SEM; $n = 6$–12. (*E*) Comparison of the healing times (scab falling off) in the days after wounding. Data are shown as means ± SEM; $n = 12$. $^{*}P < 0.05$; $^{**}P < 0.01$; $^{***}P < 0.001$.

and adult mice (21, 22). In findings related, to some extent, to these results, the requirement for functional vimentin in epithelial maintenance was demonstrated by recent observations showing that compromised vimentin phosphorylation caused cellular senescence in lens epithelial cells (23), cytokinetic failure of s.c. fibroblasts upon injury (24), and skin aging (24). These studies were made in phospho-vimentin–deficient mice in which all mitotic serine-specific phosphorylation sites were replaced by alanine residues.

Because the redifferentiation following wound injury involves such a dramatic increase in vimentin expression (which has been established as a determinant of a number of signaling systems), we wanted to investigate whether vimentin could be directly involved in regulating the cellular processes and interactions that are required for proper regeneration and healing. To address this hypothesis in a physiological setting, we used a combination of two well-defined in vivo wound-healing paradigms, burn and excision injury, in genetically engineered mice lacking vimentin. Along with the in vivo experiments, we also used a number of reconstituted cellular in vitro models relevant to the wound-healing process to validate the assumptions based on observations in healing tissue. Indeed, the results show that vimentin serves as an integrator of the processes that occur during wound healing, regulating the proliferation of fibroblasts and the EMT-like transdifferentiation of keratinocytes, both crucial processes for successful wound repair. In the absence of vimentin, these cellular processes are inhibited, thereby disrupting normal tissue regeneration, reepithelialization, and the formation of a scar and an intact barrier.

Results

Loss of Vimentin Leads to Deficient Wound Healing. Burns or excisional skin wounds in mice are common experimental approaches to assess molecular, cellular, and tissue movements associated with repair. To determine whether vimentin is an important determinant in wound healing, full-thickness standardized burn wounds (1 cm in diameter) were induced in 8- to 10-wk-old VIM$^{-/-}$ mice and their WT littermates. A histological analysis of wound morphology 9 d after injury revealed epidermal healing of only 17% reepithelialization of the wounds in VIM$^{-/-}$ mice compared with 32% in the WT group (Fig. 1 *A* and *B*). At day 15 postinjury the wounds in WT mice were reepithelialized completely, with a prominent keratinized layer (Fig. 1 *A* and *B*). In contrast, the epithelium layer in VIM$^{-/-}$ mice remained open (~56% reepithelialization) and in many mice was still covered by a large scab (Fig. 1 *A* and *B*). Furthermore, the wound-closure area, quan-

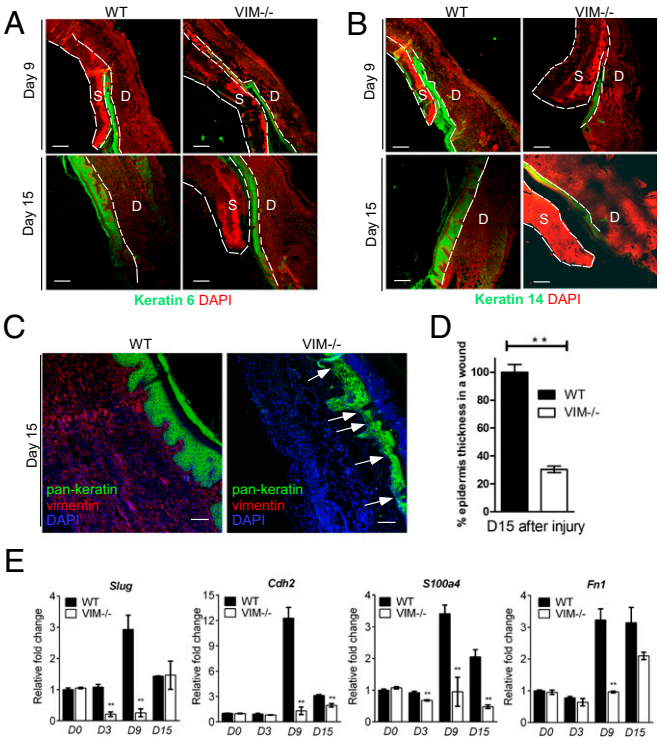

Fig. 2. Compromised reepithelialization and EMT differentiation in VIM$^{-/-}$ wounds. (*A* and *B*) Representative pictures of confocal images of keratin 6 (green) and DAPI (red) (*A*) and keratin 14 (green) and DAPI (red) (*B*) in VIM$^{-/-}$ and WT wounds on day 9 and 15 after skin burn injury. D, dermis region; S, scab region. (Scale bars, 200 μm.) (*C*) Representative confocal images of keratin expression as visualized by a pan-keratin antibody (green), vimentin (red), and DAPI (blue) in VIM$^{-/-}$ and WT wounds on day 15 postinjury. White arrows indicate the region of thin and poor keratinization in VIM$^{-/-}$ wounds. (*D*) Quantification of average epidermis thickness on day 15 after burn injury. Bars indicate the mean fold changes relative to WT ± SEM; $n = 3$. (*E*) qRT-PCR analysis of mRNA transcripts for Slug, N-cadherin (*Cdh2*), FSP-1 (*S100a4*), and fibronectin (*Fn1*) in isolated epidermal regions of VIM$^{-/-}$ and WT wounds on days 0, 3, 9, and 15 after burn injury. Bars indicate the mean fold changes ± SEM relative to day 0 WT; $^{**}P < 0.01$; $n = 3$.

tified at different time points following injury, showed that from day 4 postinjury healing was significantly slower in the VIM$^{-/-}$ group than in the WT group (Fig. 1 *C* and *D*). As shown in Fig. 1*E*, the time to healing (i.e., when the scab falls off) was ∼3 d longer in the VIM$^{-/-}$ group than in WT group. As with burn wounds, the healing of excisional wounds was severely impaired in VIM$^{-/-}$ mice (Fig. S1). To examine the possible influence of basal skin conditions on wound healing, we analyzed the overall features of uninjured control skin of prenatal mice at embryonic day 14 (E14), preweaning (18-d-old) mice, and adult mice (age 10 wk old up to 10 mo) (Fig. S2). In this examination of the uninjured skin, no striking differences in the organization of epidermis, dermis, and cell components could be observed between WT and VIM$^{-/-}$ skins (Fig. S2 *A–D*). The results demonstrate that loss of vimentin inhibits normal wound healing, resulting in a slow and incomplete recovery of the tissue.

The Defect in Reepithelialization Is Associated with an Inactive EMT Program in VIM$^{-/-}$ Wounds. To evaluate skin reepithelialization during wound healing further, we analyzed the keratinocytes at wound margins, which form a coordinated cell sheet with de novo production of injury-specific keratin proteins, such as keratin 6, 14, and 16 (25, 26). WT wounds had higher keratin 6 intensity than VIM$^{-/-}$ wounds at days 9 and 15 postinjury (Fig. 2*A*), and a similar tendency was observed for keratin 14 and with labeling by a pan-keratin antibody (Fig. 2 *B* and *C*). By day 15 postinjury, keratinocyte colonies had fused successfully with the newly formed stratified mature epidermis in WT wounds. In contrast, reepithelialized VIM$^{-/-}$ wound regions displayed a very thin epidermal layer with a large scab (right images in Fig. 2 *A* and *B*); the average thickness of pan-keratin^{+} epidermis was barely 30.5% of that in the WT group (Fig. 2*D*). Furthermore, certain regions of keratinocyte colonies in the epidermis of VIM$^{-/-}$ wounds were poorly organized (Fig. 2*C*). These observations imply that migration, maturation, and stratification of the epidermis, all prerequisites for fast, spontaneous wound healing, are severely compromised in the VIM$^{-/-}$ group.

EMT or an EMT-like transdifferentiation program induces the transient transition of secondary epithelial cells to a more migratory phenotype, which is critical for rapid reepithelialization of injured epithelium (27, 28). To address the role of vimentin in this process, we analyzed whether the absence of vimentin affects EMT during wound repair in injured epidermis. We found that during normal WT wound closure, the expression of a major EMT initiator, the transcription factor Slug (also termed Snai2), remained at the same levels found in samples of day 0 uninjured WT skin until day 3 (Fig. 2*E*). In the WT injured skin samples, the expression of Slug mRNA increased dramatically from day 0 until day 9 and then ceased by day 15 (Fig. 2*E*). In comparison, skin samples from VIM$^{-/-}$ mice showed significantly reduced mRNA expression of Slug during wound healing; we observed a 4.7-fold reduction on day 3 and a prominent 11.5-fold reduction on day 9 in the wounds of VIM$^{-/-}$ mice as compared with their WT littermates (Fig. 2*E*). On day 15, *Slug* expression returned to similar levels in WT and VIM$^{-/-}$ wounds (Fig. 2*E*), in accordance with previously observed kinetics of transient Slug induction in several skin-injury studies (3, 29). Correspondingly, the mRNA expression of EMT-dependent markers downstream of Slug, including N-cadherin (*Cdh2*), fibroblast-specific protein 1 (*S100a4*), and fibronectin (*Fn1*) (30), increased until day 9 and decreased by day 15 during normal WT wound closure (Fig. 2*E*). The baseline expression of these genes in skin samples from VIM$^{-/-}$ mice were at the same levels as in day 0 WT skin samples but dropped drastically during wound healing, especially at day 9 (Fig. 2*E*), further supporting the vimentin dependence of the Slug–EMT response during wound repair.

We also found keratin^{+} cell colonies at the WT epidermis–dermis interface that were absent in VIM$^{-/-}$ wounds at day 9 postinjury (Fig. S3 *A* and *B*). Additionally a significant portion of cells in the dermal regions of WT wounds coexpressed keratin and the mesenchymal marker α-SMA (Fig. S3*C*) at day 9 postinjury. Another mesenchymal marker, N-cadherin, was coexpressed with keratin 5 in WT epidermal cells on day 15 postinjury (Fig. S3 *E* and *F*). Such cells, which may be at the intermediate stages of EMT, with continued expression of epithelial markers but acquiring the expression of mesenchymal markers, were much less abundant in the healing VIM$^{-/-}$ skin (Fig. S3 *C–F*). Therefore, in the absence of vimentin, the consequent dysfunction of the EMT program is likely to be a primary reason for the inhibited reepithelialization during wound repair in our models.

TGF-β Derived from Dermal Fibroblasts Triggers the Slug–EMT Program and Epithelial Cell Migration. An EMT-like keratinocyte transdifferentiation program can be modulated rapidly by a variety of factors in the wound environment (31, 32). Therefore we explored the possible involvement of these signaling factors by gene-expression profiling and found that TGF-β1 (*Tgfb1*), a primary inducer of EMT,

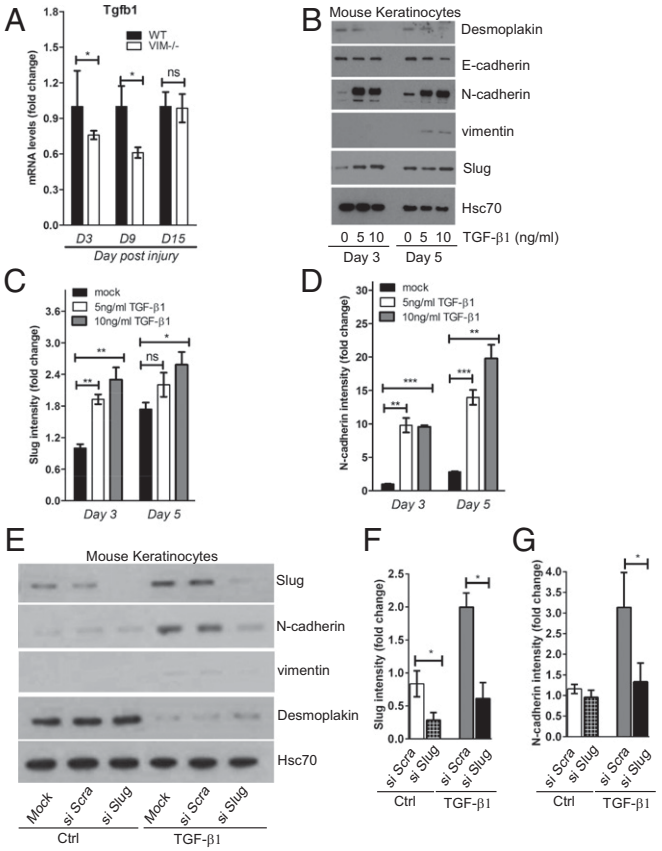

Fig. 3. TGF-β1–Slug signaling promotes keratinocyte differentiation and migration. (*A*) qRT-PCR analysis of transcripts for TGF-β1 (*Tgfb1*) in VIM$^{-/-}$ and WT wounds on days 3, 9, and 15 after wounding. Bars show mean fold changes ± SEM relative to WT; $n = 3$. (*B*) Mouse keratinocytes were stimulated with 5–10 ng/mL TGF-β1 for 0, 3, or 5 d. Cell lysates were collected and blotted with antibodies against desmoplakin, E-cadherin, N-cadherin, vimentin, and Hsc-70 as loading control. (*C* and *D*) Quantification of Slug (*C*) and N-cadherin (*D*) intensity in *B* equalized to Hsc-70. Bars show mean fold changes ± SEM relative to day 3 control mice; $n = 3$. (*E*) Mouse keratinocytes were transfected with scramble siRNA (si Scra) or Slug siRNA (si Slug) oligos for 2 d and then were stimulated with 5 ng/mL TGF-β1 for 3 d. Cell lysates were collected for Western blotting analysis of Slug, N-cadherin, vimentin, desmoplakin, and loading control Hsc-70. (*F* and *G*) Quantification of Slug (*F*) and N-cadherin (*G*) intensity in *E* equalized to Hsc-70. Bars show the mean fold changes ± SEM relative to mock transfections (Ctrl); $n = 3$; $^{*}P < 0.05$; $^{**}P < 0.01$; $^{***}P < 0.001$; ns, not significant.

had a significantly lower expression at day 3 and day 9 postinjury in VIM$^{-/-}$ wound tissues than in their WT counterparts (Fig. 3*A*). Recombinant TGF-β1 potently inhibited the expression of the epithelial markers desmoplakin and E-cadherin and induced the expression of Slug, N-cadherin, and vimentin (all hallmarks of an EMT-like transdifferentiation process) in mouse keratinocytes following cytokine stimulation (Fig. 3 *B–D*). To examine the involvement of Slug in wound healing-mediated EMT, we silenced Slug expression in keratinocytes using Slug siRNA in the absence or presence of TGF-β1 (Fig. 3 *E* and *F*). Keratinocytes transfected with Slug siRNA had reduced expression of N-cadherin and vimentin as well as a slight induction of desmoplakin upon TGF-β stimulation (Fig. 3 *E–G*), indicating that Slug is needed to induce EMT downstream of TGF-β. Taken together, these data suggest that TGF-β1 produced in WT wounds is capable of driving an active EMT transdifferentiation program via Slug.

Because vimentin as a mesenchymal marker is expressed mainly in dermal compartments, we postulated that activated dermal fibroblasts would be responsible for the TGF-β production observed upon injury, thereby triggering epidermal keratinocyte transdifferentiation. In support of this hypothesis, we found that mouse dermal fibroblasts (MDFs) isolated from VIM$^{-/-}$ mice have lower TGF-β1 gene expression than MDFs from WT mice (Fig. 4*A*). Correspondingly, the levels of active TGF-β1 in the supernatants of VIM$^{-/-}$ MDFs were significantly lower than in the supernatants of WT MDFs (Fig. 4*B*). Cell-culture supernatants of WT MDFs containing greater amounts of TGF-β1 induced a stronger EMT program in the cultivated mouse keratinocytes than did supernatants from VIM$^{-/-}$ MDFs (Fig. 4*C*). Consistently, in a scrape-wound assay, mouse keratinocytes closed the scrape wounds considerably faster in the presence of conditioned medium from WT MDFs than in conditioned medium from VIM$^{-/-}$ MDFs (Fig. 4 *D* and *E*). To exclude the involvement of other cellular effectors of inflammation that might be relevant to the keratinocyte phenotype, we assessed the expression of key cytokines and the presence of inflammatory cells during wound repair. We found that the expression of the mRNA of proinflammatory cytokines IL-6 (*Il6*), IL-1α (*Il1a*), IL-1β (*Il1b*), IL-23 (*Il23*), and TNF-α (*Tnf*) remained at similar levels (less than 1.5-fold changes) between WT and VIM$^{-/-}$ wounds on day 3 and day 9 postinjury (Fig. S4*A*). Although on day 9 postinjury, 1.5-fold fewer neutrophil cells had infiltrated to the edges of WT wounds than to the edges of VIM$^{-/-}$ wounds (Fig. S4 *B* and *C*), there was no significant change in the myeloperoxidase activity of neutrophils (MPO^{+}) in WT and VIM$^{-/-}$ wounds at day 9 postinjury (Fig. S4 *D* and *E*). In addition, the presence of macrophages (CD11b^{+}) and activated T cells (Zap-70^{+}) was comparable between WT and VIM$^{-/-}$ wounds on day 9 of wound repair (Fig. S4 *D* and *E*). Cell-culture supernatants of WT and VIM$^{-/-}$ macrophages also contained equal levels of TGF-β1 (Fig. S4*F*), demonstrating that the loss of vimentin in the regional fibroblasts, but not the infiltrated inflammatory cells, is the key effector of insufficient TGF-β production and signaling.

To test further whether TGF-β1 produced from MDFs is required to drive EMT-like changes in keratinocytes, a pan–TGF-β neutralizing antibody, 1D11, and two chemical inhibitors of TGF-β receptors, LY2109761 and SB431542, were added to MDF-conditioned medium; all effectively inhibited the phosphorylation of Smad2/3 (Fig. 4*F*), downstream effectors of the TGF-β signaling pathway. Further corroborating the involvement TGF-β signaling were the results showing that when TGF-β signaling was blocked, the expression of EMT markers (Slug and N-cadherin) in keratinocytes was reduced (Fig. 4 *G* and *H*), and cell migration was inhibited (Fig. 4*I*). This effect was prominent in cells incubated in the presence of WT MDF supernatants (Fig. 4 *G–I*), which contained higher levels of active TGF-β1 than VIM$^{-/-}$ MDF supernatants (Fig. 4*B*), reinforcing the notion that TGF-β signaling is a major driver in keratinocyte transdifferentiation and migration induced by fibroblast vimentin. Inhibition of Slug expression by siRNA in keratinocytes also inhibited cell migration (Fig. 4*J*), further demonstrating that vimentin regulates keratinocyte migration through *TGF-β* –Slug signaling.

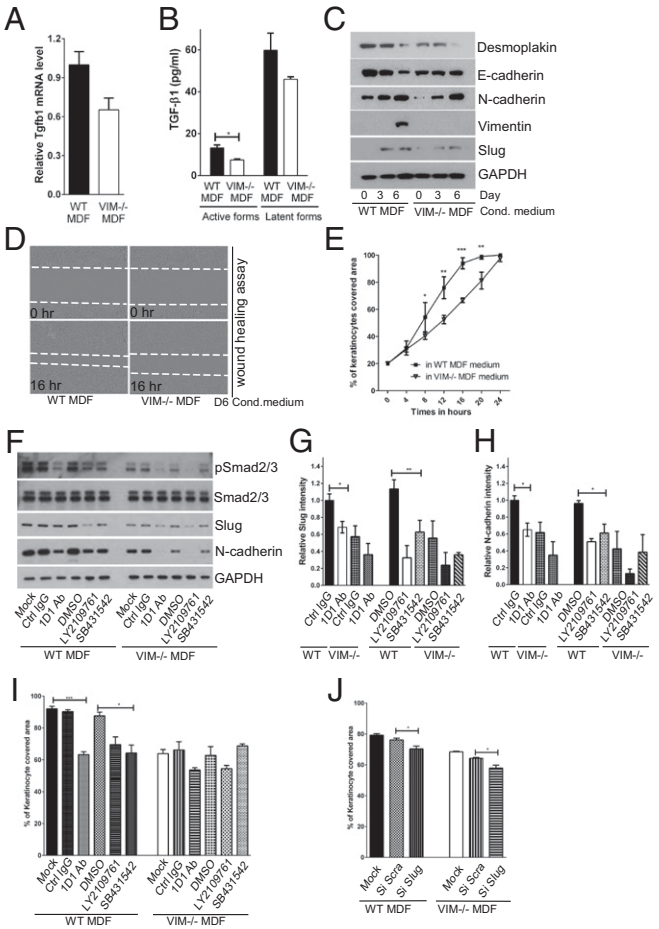

Fig. 4. Vimentin promotes TGF-β production from fibroblasts driving EMT and migration of keratinocytes. (*A*) qRT-PCR analysis of transcripts for TGF-β1 (*Tgfb1*) in VIM$^{-/-}$ and WT MDFs. Bars show mean fold changes ± SEM relative to WT; $n = 6$. (*B*) Level of active and latent forms of TGF-β1 in the supernatants of 6-d MDF cell cultures were analyzed by ELISA. Data are shown as mean ± SEM; $n = 3$. (*C*) VIM$^{-/-}$ and WT MDF cell-culture media were extracted on 0, 3, and 6 d after cell growth. The growth medium of mouse keratinocytes was replaced with the MDF-conditioned medium for 5 d. Cell lysates were collected and blotted with antibodies against desmoplakin, E-cadherin, N-cadherin, vimentin, Slug, and loading control GAPDH. (*D* and *E*) In vitro wound-healing assay of mouse keratinocytes grown in 6-d conditioned medium from VIM$^{-/-}$ MDFs and WT MDFs. The cell gap was monitored over 24 h, and the wound areas were measured and plotted against the time point. At least four wound scratches were analyzed per experiment. Data are shown as means ± SEM; $n = 3$. (*F*) Mouse keratinocytes grown in 6-d conditioned medium from the VIM$^{-/-}$ and WT MDFs were treated with control IgG (Ctrl IgG, 10 μg/mL), pan–TGF-β neutralizing antibody 1D11 (1D1 Ab, 10 μg/mL), two chemical inhibitors of TGF-β receptors [LY2109761 (2 μM) and SB431542 (2 μM)] or were grown in the corresponding DMSO control (DMSO, 2 μM) for 3 d. The cell lysates from this experiment were blotted with antibodies against pSmad2/3, total Smad2/3, Slug, N-cadherin, and loading control GAPDH. (*G* and *H*) Quantification of Slug and N-cadherin intensity in *F* equalized to GAPDH; bars show the mean fold changes relative to WT Ctrl IgG ± SEM; $n = 3$. (*I*) In vitro wound-healing assay of mouse keratinocytes (at 16 h of wound healing) in the treatments in *F*. (*J*) The *y* axis shows the percentage of area covered (at 16 h of wound healing) by keratinocytes transfected with mock, scramble siRNA (si Scra), or Slug siRNA (si Slug) oligos for 2 d and incubated in 6-d WT or VIM$^{-/-}$ MDF-conditioned medium. In *I* and *J*, at least four wound scratches were analyzed per experiment. Data are shown as means ± SEM; $n = 3$; $^{*}P < 0.05$; $^{**}P < 0.01$; $^{***}P < 0.001$.

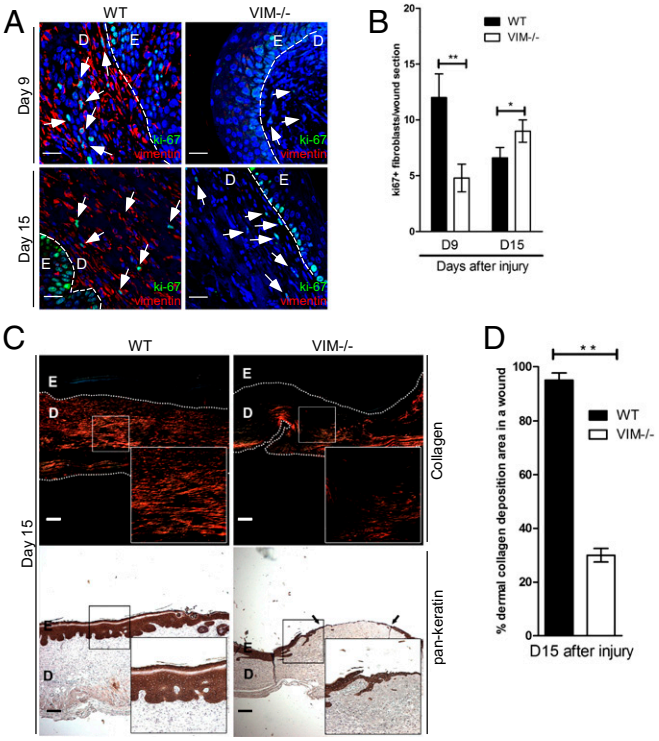

Fig. 5. Vimentin promotes mesenchymal cell proliferation and collagen accumulation in vivo. (*A*) Representative confocal images of the expression of Ki67 (punctate green signal in the nucleus) and vimentin (red) in VIM$^{-/-}$ and WT wounds on days 9 (D9) and 15 (D15) after burn wounding. Nuclei were counterstained with DAPI (blue). (Scale bars, 20 μm.) The white arrowheads indicate examples of ki67^{+} cells in dermal regions. D, dermis region; E, epidermis region. (*B*) Quantitation of ki67^{+} cells in mesenchymal/dermal regions of wounds. (*C*) Representative pictures of Picro-Sirius Red staining of collagen (*Upper*) and the immunohistochemical labeling of pan-keratin (*Lower*) in the corresponding sections of VIM$^{-/-}$ and WT wounds on day 15 postinjury. The right lower corner of each panel shows an enlarged image of the area in the white box. (Scale bars, 100 μm.) (*D*) The quantitation of collagen accumulation (Picro-Sirius Red-positive areas) in mesenchymal/dermal regions of wounds. In *B* and *D* data are shown as means ± SEM; $n = 3$; $^{*}P < 0.05$; $^{**}P < 0.01$.

Vimentin Promotes Fibroblast Proliferation, Collagen Accumulation, and Paracrine EMT Signals. At later stages of tissue repair, we found that the VIM$^{-/-}$ wounds displayed a striking reduction in s.c. proliferating fibroblasts, as indicated by the loss of cells positive for the proliferation marker nuclear antigen ki67 (Fig. 5 *A* and *B*). To assess whether this fibroblast deficiency would lead to a defect in ECM synthesis and buildup, we analyzed the accumulation of dermal collagen using Picro-Sirius Red staining (33). The normal granulation tissue with thick collagen fibers that was observed in WT wounds could not be observed in VIM$^{-/-}$ wounds, which instead showed either no fibers or at best a few scattered thin fibers (Fig. 5*C*). At 15 d postinjury, a striking difference was observed between WT and VIM$^{-/-}$ wounds: Collagen accumulation was largely absent in the dermal regions of VIM$^{-/-}$ wounds, whereas the majority (~95%) of WT dermis was occupied by collagen fibers (Fig. 5*D*). There was no striking difference in collagen accumulation between normal, uninjured WT and VIM$^{-/-}$ adult skins (Fig. S2 *E* and *F*, 10 wk), excluding the possibility of a problem in s.c. collagen distribution in uninjured basal skin. Therefore the collagen defect can be attributed entirely to events during wound healing, and the observed absence in reepithelialization in VIM$^{-/-}$ wounds is closely associated with the inhibition of fibroblast proliferation and collagen accumulation.

To investigate further whether vimentin plays a direct role in dermal fibroblast proliferation, we compared the proliferative potential of VIM$^{-/-}$ and WT MDFs. The results showed that VIM$^{-/-}$ MDFs grew much more slowly than WT MDFs (Fig. 6*A*), although the apoptotic rates in VIM$^{-/-}$ and WT MDFs were similar (Fig. S5*A*). To determine whether vimentin expression is required for the growth advantage, exogenous vimentin construct was titrated into VIM$^{-/-}$ MDFs. We found that reconstitution of vimentin in VIM$^{-/-}$ MDFs restored the cell proliferation capacity in a dose-dependent manner (Fig. 6*A*) that was associated with the reactivation of ERK1/2 signaling (Fig. 6*B*). Furthermore, the conditioned medium from these VIM$^{-/-}$ MDFs reexpressing increasing levels of vimentin gradually rescued the EMT and migration defect in keratinocytes (Fig. 6 *C* and *D*). These results suggest that the presence of vimentin in fibroblasts not only directly regulates the proliferation of these cells but also drives the transdifferentiation of keratinocytes by TGF-β1–mediated paracrine mechanisms.

Taking these results together, we have been able to validate the conceptual framework derived from in vivo observations by in vitro experiments with dermal fibroblasts and keratinocytes isolated from VIM$^{-/-}$ and WT mice. Our working model summarized in Fig. 6*E* proposes that vimentin orchestrates wound healing by regulating fibroblast proliferation and thereby both collagen accumulation and the TGF-β1–mediated Slug–EMT switch in keratinocytes.

Discussion

In this study we have demonstrated that vimentin directly coordinates four cellular activities important in the control of wound healing: fibroblast proliferation, collagen accumulation, keratinocyte transdifferentiation, and reepithelialization. Loss of vimentin disrupts this coordination, leading to slow, poor, and incomplete wound healing. Because burn and excisional wound models are very different in their character, our data demonstrate that vimentin has a general role in determining the progression of epidermal regeneration regardless of the type of epidermal injury.

TGF-β has been shown to modulate integrin expression of keratinocytes toward a more migratory phenotype (34), suggesting its supportive role in reepithelialization. TGF-β occupies a central position in the EMT signaling networks, including MEK/ERK, JNK/p38, MAP kinases, Rho GTPase, and PI3K/Akt signaling pathways (6). Vimentin plays an active role in the cellular partners that receive EMT-inducing signals (9, 10, 12), as demonstrated by previous studies showing the vimentin dependence of EMT in a cancer context and our recent observations in TGF-β1–responsive mammary epithelial (MCF10A) cells (10, 12). Because vimentin was required for the observed EMT phenotype, a common paradigm might be that vimentin, by being involved in the regulation of both TGF-β signal triggering and reception, orchestrates a dynamic balance of epithelial–stromal (epidermal–dermal) signals that induce EMT-like differentiation processes. This paradigm may be relevant not only for skin wound healing but also other physiological conditions that involve EMT.

We found that there is a kinetic expression of Slug and downstream EMT genes during normal WT wound closure. Our data imply that in WT skin these EMT genes normally are kept at a steady state in the beginning of the proliferation phase during the healing process (day 3), whereas in VIM$^{-/-}$ skin the expression of Slug drops completely. At day 9, all EMT genes are strongly induced in WT skin, but in VIM$^{-/-}$ skin, there is little or no induction and Slug remains suppressed at the day 3 level. These results emphasize the vimentin dependence of the Slug response in wound healing, as we have demonstrated previously in the context of a cancer model (12). Interestingly, after 15 d of recovery, Slug expression in VIM$^{-/-}$ skin was restored to the same levels as in WT skin. One can speculate that, in addition to the TGF-β–vimentin signaling pathway outlined in this study,

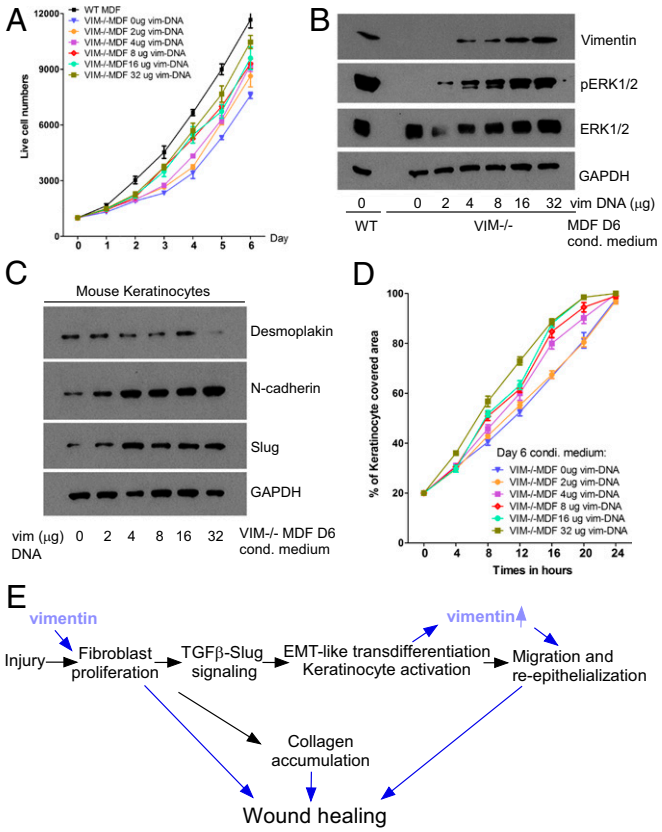

Fig. 6. Vimentin promotes mesenchymal cell proliferation and paracrine EMT signaling in vitro. (*A*) The growth curve of VIM$^{-/-}$ and WT MDF cells after transfected with different amounts of vectors encoding full-length vimentin (the total DNA per transfection was equalized with the control vector). Data are shown as mean ± SEM; $n = 3$. (*B*) Immunoblotting of vimentin, pERK1/2, total ERK1/2, and GAPDH expression of the cell lysates in *A*. (*C* and *D*) Western blotting of individual markers (*C*) and migration (*D*) of mouse keratinocytes growing in 6-d conditioned medium (D6) from VIM$^{-/-}$ and WT MDFs transfected with the indicated amount of vimentin plasmids. Data are shown as means ± SEM; $n = 3$. (*E*) Scheme showing the working model. Vimentin has a profound effect on fibroblast proliferation, which activates both collagen production and TGF-β secretion. The active fibroblast TGF-β induces Slug–EMT signaling in keratinocytes, promoting EMT-like transdifferentiation and keratinocyte migration.

Slug expression may be stimulated by other signaling modalities that could set in at this late stage to compensate for the lack of TGF-β–mediated stimulation. The dramatic induction of Slug mRNA in WT skin on day 9 postinjury that returned to normal levels when the healing was completed on day 15 is consistent with previous observations from an in vitro wound-healing model that described a transient induction of Slug with a subsequent decline upon healing of the wound (29). Thus we speculate that Slug is involved mainly in the events in the early stage of wound reepithelialization, such as triggering EMT during the proliferation phase.

We have shown previously that silencing Slug in a breast cancer model reduces vimentin expression (12). Interestingly, a recent report also revealed that keratinocytes transfected with Slug siRNA showed reduced expression of vimentin and inhibited cell migration (35). In the present study we provide further evidence demonstrating that Slug is a key mediator of TGF-β–induced expression of vimentin and other EMT markers in keratinocytes, accelerating cell migration. Our data indicate that vimentin regulates the proliferation of s.c. fibroblasts through ERK signaling; this notion is supported by our recent study on the molecular mechanisms underlying the vimentin-mediated control of growth factor signaling in the breast cancer model (12). Our current data show that the vimentin-dependent TGF-β–Slug–EMT signaling has a very steep dose–response curve, because a low level of exogenously expressed vimentin was already sufficient to rescue pERK signaling, MDF proliferation, Slug–EMT signaling, and keratinocyte migration. These results also are consistent with our previous finding that reintroducing of low levels of vimentin could fully restore EMT–ERK–Slug axis signaling in the breast cancer model (12). Taken together, our results show that the Slug–vimentin signaling axis in wound healing-related EMT is surprisingly similar to the EMT signaling we observed in the breast cancer model. Vimentin expression is dependent on Slug, and vice versa, and both contribute to ERK activation.

Vimentin-deficient wounds were conspicuously devoid of collagen accumulation, apparently as a direct consequence of the severe inhibition of fibroblast proliferation and expansion. In fact, a recent study indicated that vimentin can contribute to the posttranscriptional regulation of collagen expression (36). Furthermore, EMT also can activate fibroblasts to produce ECM (27). Based on our results, we speculate that both the slower proliferation rate of vimentin-deficient fibroblasts and the impaired EMT-like transdifferentiation of keratinocytes contribute to reduced collagen production and the observed delayed wound-healing phenotype.

Interestingly, although there were comparable levels of cytokine expression, myeloperoxidase activity of neutrophils, and macrophage and T-cell infiltration in the injured sites of WT and VIM$^{-/-}$ skin in the early stage of the healing process, we observed elevated and sustained expression of inflammatory cytokines (IL-6, IL-1α, IL-1β, IL-23, and TNF-α) at the late stage of VIM$^{-/-}$ wounds (day 15 postinjury) that correlates to a prolonged neutrophil infiltration in the VIM$^{-/-}$ wound edges. This prolonged inflammation may be a compensation mechanism in which the tissue attempts to drive healing of the VIM$^{-/-}$ wound. This hypothesis is supported by our preliminary observations showing that, although complete wound closure seemed to be achieved eventually (>20–25 d after wounding) in VIM$^{-/-}$ mice, the reepithelialization was still incomplete, as already reflected in the weak reepithelization of Vim$^{-/-}$ skin at day 15 postinjury. Future studies to assess the role of chronic inflammation in terminal healing will be warranted to understand better the possible contribution of inflammation and immune response determinants to the VIM$^{-/-}$ repair phenotype.

Recent research has rapidly expanded the knowledge of the functions of vimentin intermediate filament proteins, including their involvement in tissue repair. When organ and tissue homeostasis has been challenged in a number of different organs, vimentin has been found to participate in many processes crucial for tissue repair and regeneration, including cell migration, proliferation, differentiation, angiogenesis, extracellular matrix remodeling, and immune responses. Obviously, epidermal wound healing features many of these cellular functions. In this respect, our study demonstrates the involvement of vimentin-mediated signaling in some of the most essential aspects of the whole healing process. The results suggest that in physiological repair systems vimentin-mediated signaling is a likely target for multifactorial orchestration of the healing process. This paradigm and this model system will be a fruitful ground to explore in greater detail the molecular and cellular mechanisms that underlie signal integration in tissue repair.

Materials and Methods

Animals. All studies involving animals are reported in accordance with the Animal Research: Reporting of In Vivo Experiments (ARRIVE) guidelines for reporting experiments involving animals (37, 38). Before and during the experiments the animals were kept under standard laboratory conditions, with a 12-h light/12-h dark cycle initiated at 0600 hours, and were supplied with chow and water ad libitum. All animals were killed by cervical dislocation. All experimental protocols for the animal experiments were approved by the Umeå University Ethical Committee for Animal Studies

(A 143-00). Vimentin heterozygous mice (129/Sv × C57BL/6) were used to generate vimentin-deficient homozygotes ($VIM^{-/-}$) and WT offspring (20). The genotypes of the mice were determined by PCR genotyping methods. Eight- to ten-week-old littermates of randomly mixed sex were used for the wound-healing experiments. Ages and sex of mice used in the experiments are summarized in Table S1.

Experimental Procedures. The mice were anesthetized by i.v. injection of 100 mL of a mixture containing 5% Ketaminol Vet (Intervet) and 20% Dormitor Vet (Orion Pharma). The hair of the back of the mouse was shaved with an electric clipper followed by a depilatory cream. To make a burn wound, a metal rod (25 g, 1 cm in diameter) was heated to 95–100 °C by submersion in boiling water. The rod was immediately positioned vertically for 6 s without additional pressure on the back skin of mice that had also been depilated 3 d before wounding. To make an excisional wound, the skin was rinsed with alcohol, and full-thickness wounds extending through the panniculus carnosus were made on the dorsum on each side of midline, using an 8-mm biopsy punch. After wounding, the mice were caged individually, and the wounds were not dressed. Only Fig. 6 and Fig. S1 include dermal excisions; all other injury analyses are from burn wounds.

Measurements of Wound Contraction and Reepithelialization. Digital photographs were taken at the day of surgery and every day after wounding. A circular reference was placed alongside to permit correction for the distance between the camera and the animals. The wound area was calculated in pixels with ImageJ 1.41 software (NIH), corrected for the area of the reference circle, and expressed as percentage of the original area. Reepithelialization was defined as the area within the pan-keratin marks that was covered with epithelium. This area was calculated by scanning the slides and measuring the epithelial tongues from the computerized image using ImageJ. The percentage of reepithelialization was determined using the formula: [(sum of epithelial tongues)/(distance between tattoo marks)] × 100.

Morphologic and Collagen Staining. Five-micrometer-thick sections were taken perpendicular to the wounded skin from paraffin-fixed tissue samples and were processed for H&E staining. Images were taken with a DC300F digital camera attached to a DM LB microscope (Leica). Sirius Red, Fast Green, and picric acid (all from Sigma) were used in Picro-Sirius Red staining for histological visualization of collagen fibers in tissue sections under polarized light microscopy (33) at 20× magnification, and pictures were taken at a fixed exposure. Quantification of collagen was performed as previously described (39) using Image Pro Plus version 4.5.0.29 imaging software (Media Cybernetics Inc.).

Immunofluorescence and Immunohistochemistry. Immunofluorescence staining of the cells on coverslips was performed as described previously (40). For tissue sample analysis, skin samples were collected 24 h after wounding and injection. Paraffin-embedded wound tissues were sectioned (5-μm thickness) perpendicular to the wound. For immunostaining of paraffin-embedded skin samples, the samples were deparaffinized and rehydrated. After antigen retrieval with 0.1 M citrate buffer (pH 6.0), sections were blocked with 5% normal goat serum, stained with primary antibodies overnight at 4 °C and with secondary antibodies for 3 h at room temperature, and counterstained with DAPI for 10 min. For immunohistochemistry analysis of tissue sections, upon antigen retrieval, tissues were immunohistochemically stained with HRP-conjugated antibody and visualized using the ABC staining system (Vector Laboratories, Inc.). Finally, all sections were counterstained with Mayer's Hematoxylin (Histolab). Isotype- and concentration-matched primary antibodies were used as negative controls, and all were found to be negative.

Microscopic Image Acquisition and Quantification. Confocal images shown in all figures were acquired at room temperature using Zeiss Zen software on a Zeiss LSM780 confocal laser-scanning microscope (Carl Zeiss, Inc.) with the following objectives: Plan-Apochromat 10× (NA 0.45, air), Plan-Apochromat 40× (NA 1.30, oil). The following fluorochromes were used: Alexa-Fluor 488, Alexa-Fluor 594, and DAPI. Immunohistochemistry images were taken with a Leica DC300F digital camera attached to a Leica DM LB microscope (Leica) or using Pannoramic digital slide scanners (3DHISTECH Ltd.). Images were viewed and brightness and contrast were adjusted using Adobe Photoshop software. Fluorescent image quantification was processed and analyzed in a pipeline created in the BioImageXD framework (41). The pipeline detects the nuclei from the Hoechst channel and counts them. The cytoplasm of each cell was modeled with a 20-pixel ring around the nucleus. All cells present within the sectioned wounds were counted. To diminish the variance within samples, at least 10 consecutive sections from each wound sample and three to six samples per time point were counted, as indicated in the figure legends.

Cell Isolation and Cell Culture. Mouse skin keratinocytes were isolated from WT newborn mice and cultured in FAD medium (DMEM/Ham's F-12 Nutrient Mixture; 3.5:1.1) supplemented with 10% (vol/vol) Chelex-treated FCS (Invitrogen), 0.18 mM adenine, 0.5 μg/mL hydrocortisone, 5 μg/mL insulin, 100 pM cholera toxin (all from Sigma), 10 ng/mL EGF, 100 U/mL sodium pyruvate, 100 μg/mL penicillin/streptomycin, and 2 mM Glutamax (all from Invitrogen) in 5% CO_2 and 32 °C. Cells were cultured on collagen I (rat tail; Invitrogen)-coated cell-culture dishes in 5% CO_2 at 32 °C. The purity of keratinocytes was confirmed by immunofluorescence (Fig. S5*B*), although low-level contamination by vimentin-expressing, nonkeratinocyte cells such as melanocytes may occur in primary cultures because of the limitations of isolation and purification techniques. MDFs were isolated from WT and $VIM^{-/-}$ newborn mice and cultured in DMEM (4.5 mM glucose) supplemented with 2 mM L-glutamine, 100 IU/mL penicillin and streptomycin, and 10% heat-inactivated FBS (Invitrogen) in 5% CO_2 at 37 °C. WT and $VIM^{-/-}$ bone marrow cells were isolated and differentiated to obtain primary murine macrophage cells using L Cell conditioned medium. Macrophages were cultured in DMEM/F12 medium supplemented with 2 mM L-glutamine, 100 IU/mL penicillin and streptomycin, and 10% heat-inactivated FBS (Invitrogen) in 5% CO_2 at 37 °C. Only cells between passages 2–9 were used for the experiments.

Antibodies and Reagents. The following antibodies were used in this study: rabbit antibodies against Slug (C19G7), vimentin (D21H3), p44/42 MAPK (Erk1/2) (137F5), phospho-p44/42 MAPK (Erk1/2) (Thr202/Tyr204), Smad2/3 (D7G7), phospho-Smad2 (Ser465/467)/Smad3 (Ser423/425) (D27F4), Zap-70 (99F2), and GAPDH (14C10) (all from Cell Signaling); Pan-keratin (Abcam), Ki67 (Abcam), N-cadherin (EPR1792Y) (Millipore), MPO (Thermo Scientific), and keratin 5 (AF 138) (Covance); rat anti–E-cadherin (GeneTex), rat anti-CD11b (AbD Serotec), rat anti-Hsc70 (Abcam); chicken anti-vimentin (Covance), and mouse anti-α-SMA (BD). Antibodies against mouse keratin 6, keratin 14, and desmoplakin were gifts from Thomas Schulz, University Leipzig, Leipzig, Germany. Growth factors and inhibitors used in this study included TGF-β1 (R&D Systems), SB 431542 (Tocris Bioscience), and LY2109761 (Santa Cruz Biotechnology).

Cell Transfection. WT and $VIM^{-/-}$ MDFs were electroporated and were transfected with different amounts of pcDNA3-vimentin (full-length) plasmids with additional amounts of backbone plasmid DNA added to keep the total plasmids consistent in every transfection. For siRNA silencing, keratinocytes were plated on a 24-well plate (50,000 cells per well). For each well, 50 nM siRNA (in one Eppendorf tube) were transfected using Lipofectamine RNAiMAX Reagent (Invitrogen). The experiments were performed a few days after transfection as indicated in *Results* and in the figure legends. Slug siRNAs (ON-TARGET plus Mouse Snai2 siRNA-SMARTpool; Dharmacon) and scrambled siRNAs (AllStars Negative Control; Qiagen) were used in this study. The siRNA Slug (Snai2) oligo sequences are listed in Table S2.

Wound-Healing Assay. For in vitro wound-healing assays, cells were grown in automated 96-well cell-migration plates and imaged with IncuCyte live-cell imaging instruments (Essen BioScience). Scratch wounds were made using a 96-pin wound-making tool (WoundMaker; Essen BioScience). Mitomycin C (10 μg/mL) was included in the medium to prevent cell proliferation. The relative migration of the cells was calculated from IncuCyte analysis software and from the area measured after scratching relative to the basal area as expressed in pixels using ImageJ 1.32 (NIH) software.

Western Blot Analysis. Cells were washed three times with TBS and were lysed in SDS/PAGE loading buffer. Cells were scraped using a sterile cell scraper and then were aspirated into a fresh 1.5-mL microcentrifuge tube and boiled at 95 °C for 5 min. Protein was separated by SDS/PAGE using 10% gel at 120 V for 90 min. After separation, protein was transferred to a nitrocellulose membrane by wet transfer at 100 V for 30 min. The nitrocellulose membrane with the transferred protein was incubated in TBS containing 5% milk and 0.3% Tween 20 for 1 h at room temperature. The membrane was washed three times in 0.3% Tween 20/TBS. The membrane was incubated with primary antibodies overnight at 4 °C with shaking. The membrane was washed three times (10 min each) in 0.3% Tween 20/TBS, was incubated again with secondary antibodies for 1 h at room temperature with shaking, and then was washed three times (10 min each) in 0.3% Tween 20/TBS. Amersham ECL reagent was used to detect protein in accordance with the manufacturer's instructions.

ELISA Analysis. The filtered MDF or macrophage cell supernatant was used to determine the TGF-β1 level by a Human/Mouse TGF beta 1 ELISA Ready-SET-Go! kit (eBioscience) according to the manufacturer's instructions. For total TGF-β1 measurement, samples were first treated with 1N HCl (1 μL/50 μL supernatant) for 15 min at room temperature and were neutralized with an equal amount of 1N NaOH before analysis in the ELISA. For active TGF-β1 measurement, samples were analyzed in the ELISA without acid treatment. Active TGF-β1 was subtracted from the total TGF-β1 to determine the latent TGF-β1 values.

Quantitative Real-Time PCR. Total RNA was extracted from skin epidermal regions using the FFPE Total RNA Isolation Kit (Invitrogen) or from cells using RNeasy mini kits (Qiagen). cDNA was obtained by reverse-transcribing same amount of total RNA using the High Capacity cDNA Reverse Transcription Kit (Applied Biosystems). The transcript levels of the genes of interest were measured by quantitative RT-PCR (qRT-PCR). The qRT-PCR reactions were performed using the SYBR Green qRT-PCR reagents (Applied Biosystems) in an Applied Biosystems 7300 detection system (Bio-Rad). The quality of the quantitative PCR run was determined by standard curves and melting-curve analysis. The data were normalized to the expression of a cellular housekeeping gene, *GAPDH*. Forward and reverse primer sequences used in this study are listed in Table S3.

Statistical Analysis. The results are expressed as the mean ± SEM. Statistical differences between groups were calculated with the two-tailed unpaired *t* test, and differences were considered significant at $P \leq 0.05$. For statistical evaluation of qRT-PCR data, logarithmic values were converted to ΔΔCt values (linear $\log_2$ scale values), and *P* values were calculated using one-tailed unpaired Student's *t* test, based on the data normalized to the appropriate control.

ACKNOWLEDGMENTS. We thank H. Saarento and C. Oram for excellent technical assistance and Dr. T. Magin, Dr. D. Granville, and Dr. K. Seltmann for providing the reagents, equipment, and software needed to complete this work. This study was supported by the Academy of Finland, the Sigrid Juselius Foundation, the Endowment of Åbo Akademi University, and Swedish National Cancer Foundation Grant 150319. F.C. was supported by a postdoctoral grant from the Academy of Finland and by Åbo Akademi University, the Finnish Cultural Foundation, and the Alfred Kordelin Foundation.

1. Gurtner GC, Werner S, Barrandon Y, Longaker MT (2008) Wound repair and regeneration. *Nature* 453(7193):314–321.
2. Reinke JM, Sorg H (2012) Wound repair and regeneration. *Eur Surg Res* 49(1):35–43.
3. Hudson LG, et al. (2009) Cutaneous wound reepithelialization is compromised in mice lacking functional Slug (Snai2). *J Dermatol Sci* 56(1):19–26.
4. Windoffer R, Beil M, Magin TM, Leube RE (2011) Cytoskeleton in motion: The dynamics of keratin intermediate filaments in epithelia. *J Cell Biol* 194(5):669–678.
5. Raja SK, Sivamani K, Garcia MS, Isseroff RR (2007) Wound re-epithelialization: Modulating keratinocyte migration in wound healing. *Front Biosci* 12:2849–2868.
6. Thiery JP, Acloque H, Huang RYJ, Nieto MA (2009) Epithelial-mesenchymal transitions in development and disease. *Cell* 139(5):871–890.
7. Hanahan D, Weinberg RA (2011) Hallmarks of cancer: The next generation. *Cell* 144(5):646–674.
8. Ivaska J, Pallari HM, Nevo J, Eriksson JE (2007) Novel functions of vimentin in cell adhesion, migration, and signaling. *Exp Cell Res* 313(10):2050–2062.
9. Mendez MG, Kojima S, Goldman RD (2010) Vimentin induces changes in cell shape, motility, and adhesion during the epithelial to mesenchymal transition. *FASEB J* 24(6):1838–1851.
10. Vuoriluoto K, et al. (2011) Vimentin regulates EMT induction by Slug and oncogenic H-Ras and migration by governing Axl expression in breast cancer. *Oncogene* 30(12):1436–1448.
11. Dave JM, Bayless KJ (2014) Vimentin as an integral regulator of cell adhesion and endothelial sprouting. *Microcirculation* 21(4):333–344.
12. Virtakoivu R, et al. (2015) Vimentin-ERK signaling uncouples Slug gene regulatory function. *Cancer Res* 75(11):2349–2362.
13. Shirley SH, Hudson LG, He J, Kusewitt DF (2010) The skinny on Slug. *Mol Carcinog* 49(10):851–861.
14. Savagner P (2001) Leaving the neighborhood: Molecular mechanisms involved during epithelial-mesenchymal transition. *BioEssays* 23(10):912–923.
15. Yilmaz M, Christofori G (2009) EMT, the cytoskeleton, and cancer cell invasion. *Cancer Metastasis Rev* 28(1-2):15–33.
16. Menko AS, et al. (2014) A central role for vimentin in regulating repair function during healing of the lens epithelium. *Mol Biol Cell* 25(6):776–790.
17. Müller M, et al. (2009) Dominant cataract formation in association with a vimentin assembly disrupting mutation. *Hum Mol Genet* 18(6):1052–1057.
18. Bornheim R, et al. (2008) A dominant vimentin mutant upregulates Hsp70 and the activity of the ubiquitin-proteasome system, and causes posterior cataracts in transgenic mice. *J Cell Sci* 121(Pt 22):3737–3746.
19. Nieminen M, et al. (2006) Vimentin function in lymphocyte adhesion and transcellular migration. *Nat Cell Biol* 8(2):156–162.
20. Colucci-Guyon E, et al. (1994) Mice lacking vimentin develop and reproduce without an obvious phenotype. *Cell* 79(4):679–694.
21. Eckes B, et al. (1998) Impaired mechanical stability, migration and contractile capacity in vimentin-deficient fibroblasts. *J Cell Sci* 111(Pt 13):1897–1907.
22. Eckes B, et al. (2000) Impaired wound healing in embryonic and adult mice lacking vimentin. *J Cell Sci* 113(Pt 13):2455–2462.
23. Matsuyama M, et al. (2013) Defect of mitotic vimentin phosphorylation causes microophthalmia and cataract via aneuploidy and senescence in lens epithelial cells. *J Biol Chem* 288(50):35626–35635.
24. Tanaka H, et al. (2015) Cytokinetic failure-induced tetraploidy develops into aneuploidy, triggering skin aging in phosphovimentin-deficient mice. *J Biol Chem* 290(21):12984–12998.
25. DePianto D, Coulombe PA (2004) Intermediate filaments and tissue repair. *Exp Cell Res* 301(1):68–76.
26. Lessard JC, et al. (2013) Keratin 16 regulates innate immunity in response to epidermal barrier breach. *Proc Natl Acad Sci USA* 110(48):19537–19542.
27. Kalluri R, Weinberg RA (2009) The basics of epithelial-mesenchymal transition. *J Clin Invest* 119(6):1420–1428.
28. Weber CE, Li NY, Wai PY, Kuo PC (2012) Epithelial-mesenchymal transition, TGF-β, and osteopontin in wound healing and tissue remodeling after injury. *J Burn Care Res* 33(3):311–318.
29. Savagner P, et al. (2005) Developmental transcription factor slug is required for effective re-epithelialization by adult keratinocytes. *J Cell Physiol* 202(3):858–866.
30. Acloque H, Thiery JP, Nieto MA (2008) The physiology and pathology of the EMT. Meeting on the epithelial-mesenchymal transition. *EMBO Rep* 9(4):322–326.
31. Kusewitt DF, et al. (2009) Slug/Snai2 is a downstream mediator of epidermal growth factor receptor-stimulated reepithelialization. *J Invest Dermatol* 129(2):491–495.
32. Zavadil J, et al. (2001) Genetic programs of epithelial cell plasticity directed by transforming growth factor-beta. *Proc Natl Acad Sci USA* 98(12):6686–6691.
33. Junqueira LCU, Bignolas G, Brentani RR (1979) Picrosirius staining plus polarization microscopy, a specific method for collagen detection in tissue sections. *Histochem J* 11(4):447–455.
34. Margadant C, Sonnenberg A (2010) Integrin-TGF-beta crosstalk in fibrosis, cancer and wound healing. *EMBO Rep* 11(2):97–105.
35. Shin JU, et al. (2015) Estrogen Upregulates Slug to Enhance the Migration of Keratinocytes. *J Invest Dermatol* 135(12):3200–3203.
36. Challa AA, Stefanovic B (2011) A novel role of vimentin filaments: Binding and stabilization of collagen mRNAs. *Mol Cell Biol* 31(18):3773–3789.
37. Kilkenny C, Browne W, Cuthill IC, Emerson M, Altman DG; NC3Rs Reporting Guidelines Working Group (2010) Animal research: Reporting in vivo experiments: The ARRIVE guidelines. *Br J Pharmacol* 160(7):1577–1579.
38. McGrath JC, Drummond GB, McLachlan EM, Kilkenny C, Wainwright CL (2010) Guidelines for reporting experiments involving animals: The ARRIVE guidelines. *Br J Pharmacol* 160(7):1573–1576.
39. Hiebert PR, Wu D, Granville DJ (2013) Granzyme B degrades extracellular matrix and contributes to delayed wound closure in apolipoprotein E knockout mice. *Cell Death Differ* 20(10):1404–1414.
40. Cheng F, et al. (2011) KSHV-initiated notch activation leads to membrane-type-1 matrix metalloproteinase-dependent lymphatic endothelial-to-mesenchymal transition. *Cell Host Microbe* 10(6):577–590.
41. Kankaanpää P, et al. (2012) BioImageXD: An open, general-purpose and high-throughput image-processing platform. *Nat Methods* 9(7):683–689.